CHEMISTRY OF MATERIALS

ARTICLE

pubs.acs.org/cm

Polymorphism and Multiferroicity in $Bi_{1-x/3}(Mn^{III}{}_3)(Mn^{III}{}_{4-x}Mn^{IV}{}_x)O_{12}$

Francesco Mezzadri,[†,*] Michele Buzzi,[‡] Chiara Pernechele,[‡] Gianluca Calestani,[†,∥] Massimo Solzi,[‡] Andrea Migliori,[§] and Edmondo Gilioli[∥]

[†]Dipartimento di Chimica GIAF, Università di Parma, Area delle Scienze 17/A, 43124 Parma, Italy

[‡]Dipartimento di Fisica, Università di Parma, Area delle Scienze 7/A, 43124 Parma, Italy

[§]IMM-CNR, Via Gobetti 101, 40129 Bologna, Italy

[∥]IMEM-CNR, Area delle Scienze 37/A, 43124 Parma, Italy

Supporting Information

ABSTRACT: We report on structural and magnetic characterizations performed on the quadruple perovskite $Bi_{1-x/3}(Mn^{III}{}_3)(Mn^{III}{}_{4-x}Mn^{IV}{}_x)O_{12}$, showing dramatic changes on the magnetic properties of different polymorphs produced by small compositional variations ($0 < x < 0.3$). Besides the stoichiometric monoclinic phase, rhombohedral ($0.10 < x < 0.27$) and cubic ($x > 0.27$) polymorphs are detected, being related to the loss of orbital ordering originated by the introduction of Mn^{4+} ions within the structure. For the monoclinic and rhombohedral phases, ferroelectric properties are suggested by single-crystal X-ray diffraction and TEM studies, while their magnetic behavior reveals weak ferromagnetism, induced by Dzyaloshinskii−Moriya (DM) interaction, characterized by high coercive fields, not easily explained by the sole DM effect. The pinning of the magnetic domains to the electric ones, mediated by strong magnetoelectric coupling, could be the mechanism at the origin of such coercive fields. This hypothesis finds further support in the low switching fields detected for the cubic phase, where just local polar character is observed.

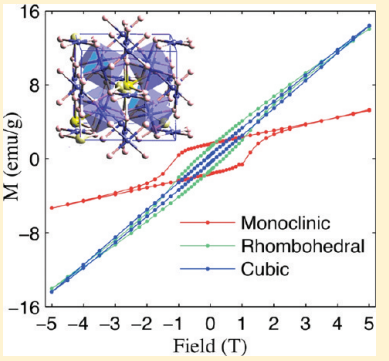

KEYWORDS: magnetoelectricity, polymorphysm, complex perovskites, manganites, $BiMn_7O_{12}$

1. INTRODUCTION

Multiferroics are interesting materials, where at least two ferroic orders (among ferroelectricity, ferromagnetism and ferroelasticity) coexist.[1] In particular, magneto-electric (ME) multiferroics could achieve a valuable technological impact, allowing the realization of multifunctional devices, exploiting more than one task at a time. Moreover, the possible presence of large ME coupling may enhance the efficiency of the existing data storage devices, raising the bit read−writing speed or allowing new degrees of freedom in spintronic devices. On the other hand, in the field of solid-state physics, understanding the conditions of coexistence of magnetism and ferroelectricity is a challenging task, while the comprehension of their complex coupling mechanisms is a completely open issue. Several perovskitic manganites (general formula $AMnO_3$) show magnetoelectric properties,[2−6] in some cases, related to large magnetoelectric coupling or multiferroicity above room temperature.

Recently, multiferroicity was hypothesized in the perovskite-related compound $BiMn_7O_{12}$, displaying weak ferromagnetism induced by Dzyaloshinskii−Moriya (DM) interaction and ferroelectric properties ascribed to the effect of the Bi(III) $6s^2$ lone pair.[7,8] The quadruple perovskite $(AA'_3B_4O_{12})$[9] structure consists of a distortion of the simple perovskitic cell, induced by a large buckling of the BO_6 coordination octahedra, with the consequent doubling of the three crystallographic axes. The A-site retains the original dodecahedral coordination typical of the simple perovskite structure, while the A′-site shows a peculiar square planar coordination, obtained as a distortion of the dodecahedral cage produced by the large buckling of the BO_6 octahedra. Therefore, the formation of the A′-site requires the presence of a Jahn−Teller active ion, such as Cu^{2+} or Mn^{3+}, the latter giving rise to the quadruple perovskite manganites with formula $(AMn_3)Mn_4O_{12}$, where the A′-site is occupied by Mn^{3+} ions, whereas the B-site can be occupied either by Mn^{3+} and Mn^{4+}, depending on the oxidation state of the ion sitting in the A-site. Several compounds with different A ions are known, displaying interesting features such as charge, orbital, and spin orderings, influencing the crystal symmetry.[10] Noteworthy is the fact that the quadruple perovskites are centrosymmetric, independently from ordering phenomena and crystal symmetry; however, the introduction of a stereochemically active ion such as Bi^{3+} on the A-site yields the loss of the inversion center,[8] giving rise to a ME compound where weak ferromagnetism is induced by DM interaction and the presence of spontaneous electrical dipole moment is ascribed to the effect of the Bi(III) $6s^2$ lone pair.

Recently, the HP synthesis of a cubic polymorph of $BiMn_7O_{12}$, by a novel synthetic route involving the use of precursors, has been reported.[11] The formation of the cubic phase would be

Received: March 28, 2011
Revised: July 15, 2011
Published: July 29, 2011

produced by partial oxidization of the B-site Mn ions, revealed by chemical analysis yielding a $Bi_{0.94}Mn_{6.91}O_{12}$ stoichiometry, where 2.6% of the total Mn ions would be oxidized to Mn^{4+}. This induced us to carry out a systematic study on the possible nonstoichiometry in the $BiMn_7O_{12}$ system, evidencing that only slight deviations from the ideal $BiMn_7O_{12}$ stoichiometry are allowed, but they dramatically affect both crystal structure and physical properties. The presence of a rhombohedral phase with intermediate composition between the monoclinic and cubic ones has been evidenced, pointing out the crucial role of the Mn^{4+} content in determining structural features and magnetic properties.

2. EXPERIMENTAL SECTION

$Bi_{1-x}Mn_7O_{12}$ polymorphs are obtained via solid-state reaction carried out under high-pressure/high-temperature (HP/HT) conditions using a multianvil apparatus, allowing the application of high hydrostatic pressure to the reactants and producing very small thermal gradients within the entire synthesis batch. MnO_2 (Alfa Aesar, 99.9%), Mn_2O_3 (Ventron, 98%), and Bi_2O_3 (Aldrich, 99.9%) are used as starting reagents; they are mixed, finely grounded, and encapsulated in Pt foils. The pressure is first increased up to 40 kbar, then the capsule is heated to 1000 °C at a rate of 50 °C/min, kept at that temperature for 2 h, and quenched to room temperature by switching off the heater. Finally, the pressure is released at ∼50 bar/min.

The samples were characterized by powder X-ray diffraction (PXRD) using a Thermo ARL X'tra diffractometer equipped with a Si(Li) Thermo Electron solid-state detector to eliminate the incoherent background produced by the fluorescence of manganese when Cu Kα radiation is used. Diffraction patterns were collected in the 2θ range of 10°−65°, with a 0.02° step and counting times ranging from 1 s to 5 s. Single-crystal XRD data were collected on a Bruker APEX II diffractometer equipped with a CCD area detector, using graphite monochromatized Mo Kα radiation. Structure solution from diffraction data was carried out using Sir2004,[12] while for the refinements, the Shelx97 program was exploited.[13] Transmission electron microscopy (TEM) measurements were performed using a Philips TECNAI F20 instrument operating at 200 kV. The specimens were prepared by grinding the powder in isopropylic alcohol and evaporating the suspension on a copper grid covered with a holey carbon film.

Energy-dispersive X-ray (EDX) microanalysis was performed using a Philips 515 scanning electron microscopy (SEM) microscope equipped with an EDAX Phoenix spectrometer with Si(Li) solid-state detector.

The magnetic characterization of the polycrystalline pellets of the three different phases was carried out by means of a MPMS-XL 5 Quantum Design superconducting quantum interference device (SQuID) magnetometer. In particular, for all of the samples, zero-field cooling (ZFC) and field cooling (FC) curves were measured in an $H = 10$ Oe applied field in the temperature range of 5−250 K and a series of hysteresis loops at different temperatures was collected for each phase. Moreover, in order to discriminate the nature of the low-temperature weak ferromagnetic order, hysteresis loops at 5 K were measured with and without high field cooling (H = 20kOe). The samples were positioned on a special made sample holder in order to avoid sample rotations when varying the magnetic field and its background signal (due to the diamagnetic sample holder) was carefully subtracted in all of the magnetization measurements. Dielectric characterization was performed on high-density polycrystalline pellets after the opposite surfaces had been polished. Using parallel-plate capacitors made from metallized mica disks, capacitance was measured with a AH 2500A 1 kHz automatic capacitance bridge while sweeping in temperature from 110 K to 5 K in zero magnetic applied field.

3. RESULTS AND DISCUSSION

3.1. Phase Diagram. A series of samples was prepared following the previously described procedure by varying the Mn_2O_3/MnO_2 ratio in the starting mixture and keeping the overall Mn/Bi ratio constant (equal to 7). The reaction products appear as dark-gray sintered powders containing single crystals with approximate dimensions of 100 μm × 100 μm × 100 μm. The samples were initially characterized by powder XRD. In analogy with ref 7, it was found that the symmetry of the quadruple perovskite increases by increasing the nominal Mn^{4+} content in the starting materials; however, besides the already known monoclinic and cubic phases, the existence of a new rhombohedral modification was noted for intermediate compositions. (For PXRD patterns of the different phases, see Figure S1 in the Supporting Information.) Monoclinic $BiMn_7O_{12}$ was obtained for Mn^{4+} content, in the starting mixture, ranging from 0% to 1.5%, in terms of molar ratio with respect to the total manganese content. PXRD evidenced the presence of small amounts of Bi_2CO_5, formed by the reaction of bismuth oxide with the CO_2 produced during the heating by the graphite furnace surrounding the platinum capsules, and Mn_2O_3. For higher Mn^{4+} contents (in the range of 1.5%−3%), a rhombohedral $BiMn_7O_{12}$ phase was detected as the main reaction product, with the sole impurities consisting of Bi_2CO_5 and Mn_2O_3 in amounts similar to the monoclinic syntheses. PXRD measurements suggest the possible coexistence of a few percent of the monoclinic phase, together with the rhombohedral one. Nonetheless, as discussed in the following, all the rhombohedral crystals checked via single-crystal XRD resulted in being single-phase, ruling out the hypothesis of post-synthesis oxidation of the samples. The further increase of the manganese(IV) content beyond 3% changes the crystallographic structure to cubic. It is interesting to note that the presence of bismuth oxycarbonate as unwanted phase increases with the increases in the amount of Mn^{4+} in the starting mixture, suggesting the presence of Mn^{4+} in the structure at the basis of the segregation of bismuth impurities. This is in agreement with the formation of A-site vacancies rather than oxygen interstitials, which also can be excluded, because of the high density of the quadruple perovskite structure.

Based on the previous considerations regarding the Bi vacancies, new syntheses were performed by changing the stoichiometry of the starting mixture following the possible formula $Bi_{1-x/3}(Mn^{III}_3)(Mn^{III}_{4-x}Mn^{IV}_x)O_{12}$, in which the presence of Mn^{4+} is fully compensated by Bi vacancies. This, on one hand, led to a reduction of Bi_2CO_5 content in the reaction products, while, on the other hand, large amounts of impurities are detected for $x > 0.5$ (in particular, unreacted Mn_2O_3), suggesting the existence of a stability limit for bismuth vacancies in the quadruple perovskite manganites, that can be overcome only by substituting Cu^{2+} ion on the A′-site, as reported for a wide series of compounds with several transition metals on the B-site.[14] The typical symmetry-dependent evolution of the XRD patterns corresponding to the three phases is reported in Figure 1, showing the distinctive

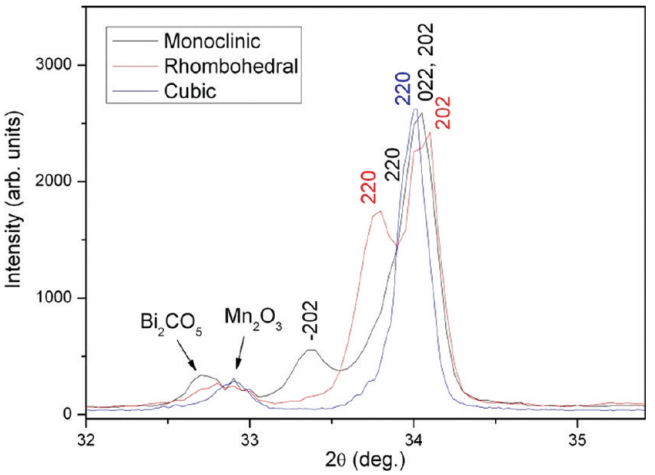

Figure 1. Typical evolution of the powder XRD pattern of the monoclinic, rhombohedral, and cubic phases. The indices of the monoclinic and rhombohedral phases refer to the pseudo-cubic cell.

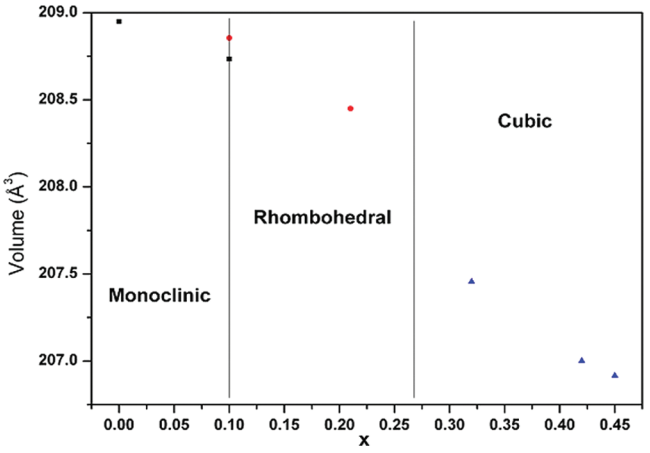

Figure 2. Volume of the primitive cell and phase diagram for the $Bi_{1-x/3}(Mn^{III}_3)(Mn^{III}_{4-x}Mn^{IV}_x)O_{12}$ system, as a function of the starting composition.

32°−35.5° 2θ region that can be considered clearly indicative of the cell symmetry. The existence domains of the three structural modifications are reported in Figure 2, as a function of the nominal Mn^{4+} content (x). The monoclinic phase was found to form in the $0 < x < 0.1$ range; for $x = 0.1$, both the monoclinic and the rhombohedral phase were formed in different experiments, indicating, for this composition, a strong dependence on slight differences in the synthesis parameters. The phase stability of the rhombohedral form extends to $x = 0.27$, the value beyond which the cubic phase is found. The symmetry increase related to the Mn^{4+} content is accompanied by a monotonic decrease of the cell volume, as reported in Figure 2.

3.2. Crystal Structure Determination. The crystal structure of the stoichiometric monoclinic phase has been determined in a previous work,[8] using single-crystal XRD performed on a small single crystal isolated from the reacted mass. In this work, the crystal structure of both the cubic and rhombohedral polymorphs was determined in the same way, the latter with the essential support of high-resolution electron microscopy (HREM). The structure of the cubic phase was solved and refined in the centrosymmetric space group $Im\bar{3}$. The Bi atom was initially refined on the cell origin with full occupancy; however, this resulted in unusually large values of the atomic displacements parameters (adps), suggesting static disorder. Therefore, Bi coordinates were allowed to move from the center of symmetry and the refinement converged with Bi atoms statistically displaced of 0.34 Å along the 3-fold axes, in agreement with ref 11. Taking into account a partial Bi deficiency to compensate the introduction of Mn^{4+} in the structure, the Bi occupancy factors were refined in the final cycles, leading to the composition $Bi_{0.94}Mn_7O_{12}$. Crystal data and refinement parameters are reported in Table S1 in the Supporting Information, and refined atomic parameters are reported in Tables S2 and S3 in the Supporting Information, whereas relevant bond distances are listed in Table S6 in the Supporting Information. Considering that the Mn1 atoms, occupying the A′-site with square planar coordination (that can be considered an extreme form of Jahn−Teller distortion), can be unambiguously considered as Mn^{3+} ions, the Mn^{4+} ions compensating the Bi deficiency should occupy the Mn2 octahedral sites. Their fraction, derived from the refined composition as 4.5% of the octahedral sites, is sufficient to remove the orbital ordering observed in the stoichiometric monoclinic phase, but not sufficient to influence significantly the Mn2−O1 bond distance that remains close to 2.00 Å, the value usually observed for Mn^{3+}. It must be noted that the refined Bi deficiency is smaller than the one expected from the starting composition ($x = 0.3$), and found by EDX analysis ($x = 0.33 \pm 0.01$). On one side, the obtained result could be, in some extent, affected by the correlation between occupancy and adps during the refinement. On the other side, the hypothesis that the real phase composition could differ slightly from the starting one is realistic, since the adjustment of the starting stoichiometry (taking into account Bi deficiency to compensate the Mn(VI) content) reduces the formation of spurious phases significantly, but it does not eliminate them completely.

The structure solution of the rhombohedral phase was undoubtedly more complicated. All the examined crystals are intrinsically twinned in a way that induced us to consider that, in the HT-HP conditions used for the synthesis, the crystal growth occurs with cubic symmetry, which is decreased to rhombohedral during the cooling process or the pressure release. At the transition, each of the four 3-fold axes of the cubic structure can survive as the unique rhombohedral axis, giving rise to four possible twinning domains, which differ in the direction of the unique axis and are slightly misoriented because of the small deviation of the cell angles from the value (109.4667°) imposed by the cubic symmetry. This was confirmed by TEM characterization showing the presence of such domains, as pointed out in Figure 3, presenting a HREM image of a twin boundary between two slightly tilted domains. As evidenced by the two insets showing the fast Fourier transforms (FFT) computed on regions belonging to different domains, the zone axis turns from [100] to [111], i.e., from a pseudo- to the true 3-fold axis of the rhombohedral structure. The TEM characterization showed a second type of twinning, occurring on a much shorter scale (extending on few tens of nanometers), giving rise to typical contrast features, evidenced in both bright-field and HREM images in Figure 4. The HREM image consists of alternating vertical strips of focused and blurred regions, indicated by arrows, that are consistent with the presence of vertical twinning boundaries canted with respect to the image plane: single-domain regions appear focused, whereas blurred regions correspond to the superimposition of two domains along

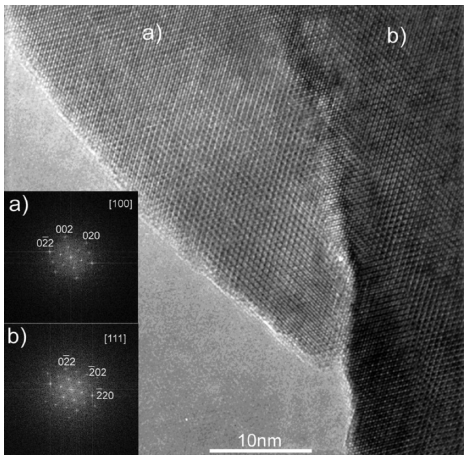

Figure 3. HREM image of a typical twin boundary in rhombohedral crystals. Fast Fourier transform (FFT) of the two domains are shown in the insets for panels a and b.

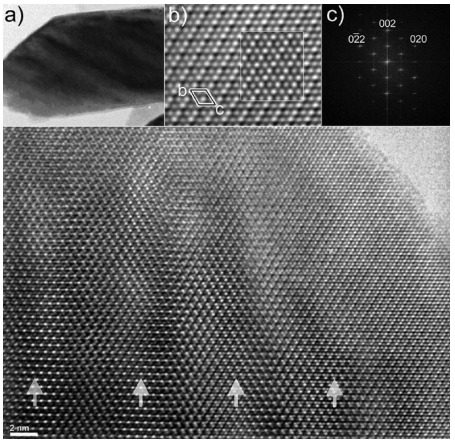

Figure 4. High-resolution electron microscopy (HREM) image of a rhombohedral sample showing polar twinning occurring at short range. Different domains are indicated by the arrows: (a) lower-resolution brigh-tfield image of the same region; (b) comparison of the experimental and calculated (t = 8.4 nm and Df = −72 nm) image of the thin region near the crystal border (the calculated image is inserted in a white frame); and (c) FFT of the entire image area.

the direction of observation. Since similar features were previously observed in the monoclinic phase and ascribed to polar twinning,[8] these observations obviously suggest also the rhombohedral phase to be ferroelectric, making the determination of the crystal structure an important step in the comprehension of the phenomenon.

A first attempt to determine the centric or noncentric character of the structure was made by refining PXRD data, but the results were not conclusive. In the case of the monoclinic polymorph, the first structure determination was performed by PXRD data in the centrosymmetric $I2/m$ space group[7] and only a further determination based on single-crystal XRD data[8] indicated the noncentric structural character described in the polar Im space group. Therefore, structure solution and refinement were addressed, in the present case, by single-crystal XRD and HREM. Fortunately, for the crystals grown under our experimental conditions, the twin domains resulting from the cubic-rhombohedral transition are

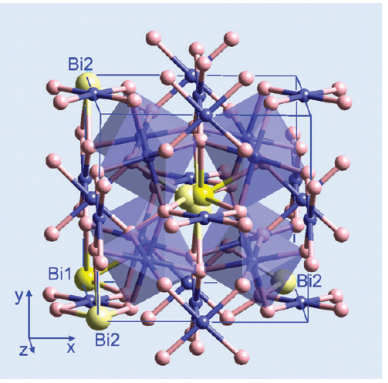

Figure 5. The refined model of the rhombohedral structure, depicted in a redundant I-centered pseudo-cubic cell for a better comprehension of the twin relationships and an easier comparison with the other polymorphic structures. The Bi ions are represented in yellow and Mn ions are shown in blue, while the O atoms are shown as being light pink.

typically nonequivalent in volume, so that the main domain can be used to determine the lattice parameters in a single-crystal XRD experiment: they were found to be a = 6.4774(16) Å and α = 109.57(3)°, in agreement with the data obtained by powder diffraction. However, with regard to the data collection, the twinning spots were too close to be separated in the integration procedure, so that the intensity data became necessarily representative of the different domains. As a consequence, intensity data were collected from different crystals for which the main twinning domain contribution was dominant. Because of this, in a first step, the structure was solved and refined without considering the twinning. Refinement in the centrosymmetric $R\bar{3}$ space group resulted, as expected, in unusually large adp values of the Bi atom (indicated as Bi1 in Figure 5), suggesting static disorder. On the other hand, by refining in $R3$, the Bi atom was found to be displaced from the origin along the 3-fold axis (indicated as Bi2 in Figure 5); however, residual electron density was found on the opposite side, around the 3-fold axis, simulating, to some extent, a disordered (but polar) displacement along the four "cubic" 3-fold axes.

Refinements of the site occupancies on data collected on different crystals clearly indicated not only the site displaced along the 3-fold axis (Bi1) to be always the most populated, but also that its occupancy factor is sample-dependent. This convinced us that this site must be considered as the real Bi position (deriving from the diffraction contribution of the dominant domain), with the other sites, distributed around the 3-fold axis, being "ghosts" related to the other twin domains.

Further support for this hypothesis was sought in the simulation of the HREM image reported in Figure 4b. As discussed previously, the contrast features of the image can be interpreted in terms of polar twinning. If the single-domain thin region near the crystal border is considered, whose enlargement is shown in the inset of Figure 4b, the HREM image can be interpreted in terms of two alternate rows of white spots running parallel to the projection of the [111]-direction on the image plane: one, which is less intense, is equally spaced along the row direction, whereas the other, which is more intense, gives rise to a sequence of differently spaced pairs in the same direction. Starting from the XRD results, an idealized model involving only Bi atoms displaced along the 3-fold axis was used for the calculation of the HREM image contrast and very good agreement between the

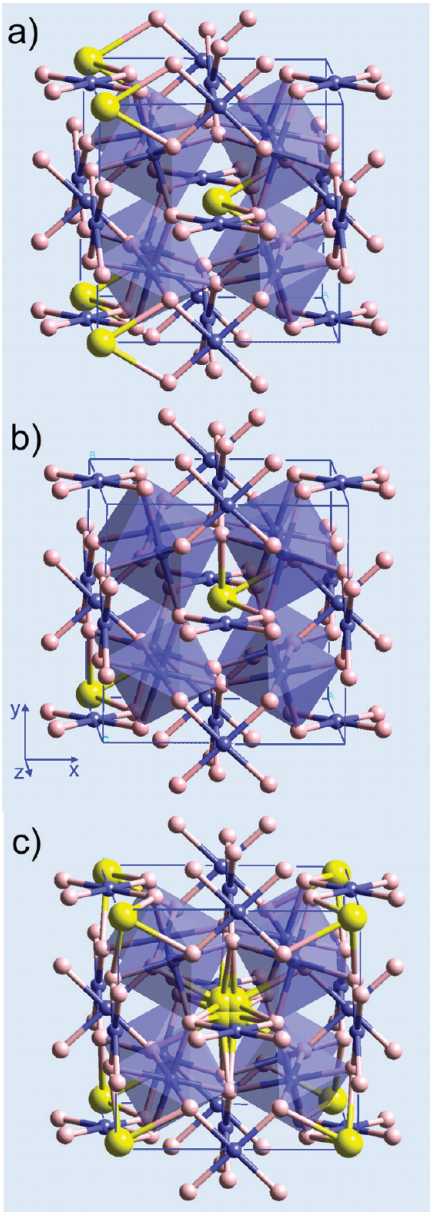

Figure 6. $BiMn_7O_{12}$ polymorphs refined structures, represented in the pseudo-cubic cell, for better understanding: (a) monoclinic phase, with Bi ions (yellow spheres) shifted along the [110]-direction; (b) rhombohedral polymorph (in this case, the polar axis corresponds to the [111]-direction); and (c) in the cubic phase, Bi ions are shifted statistically along one of the eight equivalent [111]-directions, resulting in statical disorder.

observed image and the computed image (shown in the inset) was found for a thickness $t = 8.4$ nm and a defocus $Df = -72$ nm. Under these conditions, the dots belonging to equispaced rows represent Mn columns and the others rows represent sequences of alternate Bi/Mn and Mn columns, differently spaced by the polar Bi displacement. Final structure refinement of the twinned single-crystal data was performed by considering the two possible Bi sites and refining their occupancy without applying constraints (leading to a final formula $Bi_{0.95}Mn_7O_{12}$). The refined values are in agreement with both the nominal composition ($x = 0.2$) and the EDX measurements, leading to $x = 0.18 \pm 0.01$. Crystal data and refinement parameters are reported in Table S1 in the

Table 1. Summary of Crystallographic Data of the Three $BiMn_7O_{12}$ Polymorphs

	monoclinic[a]	rhombohedral	cubic
formula	$BiMn_7O_{12}$	$Bi_{0.95}Mn_7O_{12}$	$Bi_{0.94}Mn_7O_{12}$
formula weight	785.53	775.14	774.07
space group	*Im*	*R*3	*Im*3
cell parameters			
a	7.5351(15) Å	6.4774(16) Å	7.458(4) Å
b	7.3840(15) Å	6.4774(16) Å	7.458(4) Å
c	7.5178(15) Å	6.4774(16) Å	7.458(4) Å
α (*β*)	91.225(3)°	109.57(3)°	90°
volume, *V*	418.19(15) $Å^3$	208.44(16) $Å^3$	414.8(4) $Å^3$
Z	2	1	2
D_{calc}	6.238 Mg m^{-3}	6.175 Mg m^{-3}	6.197 Mg m^{-3}

[a] Data taken from ref 8.

Supporting Information and atomic parameters in Tables S4 and S5 in the Supporting Information. The refined model is shown in Figure 5, whereas relevant bond distances are listed in Table S6 in the Supporting Information, compared to those of the cubic phase. Even if the information is mediated—at least to some extent—by twin contributions, the analysis of the Mn−O bond distances suggests that Mn^{4+} ions occupy the Mn1 octahedral sites laying on the 3-fold axis. In this hypothesis, the localization of Mn^{4+} would be at the basis of the setting of the rhombohedral crystal symmetry. A comparison of the structure of the different polymorphs is shown in Figure 6, while the structural features of the cubic and rhombohedral polymorphs, together with those previously known for the monoclinic phase, are collected in Table 1. In all cases, the main feature is represented by the distorted coordination of bismuth, giving rise to polar structures for both monoclinic and rhombohedral polymorphs. Even in the cubic case, despite the centrosymmetric character of the averaged structure, the displacement of the Bi atom forces the local structure to be acentric; however, with the diffraction response being averaged on the entire crystal, no information on the existence of a local polar character and on its coherence length becomes available. The fact that polymorphism in this system is driven by subtle changes in the phase stoichiometry involving the oxidation to Mn^{4+} of a very small fraction of the Mn^{3+} ions occupying the B-sites is surprising. Noteworthy, the crystal structure of quadruple perovskites is determined by ordering phenomena (orbital and charge) occurring on a larger scale. For example, in $NaMn_7O_{12}$, the presence of Na^+ ions in the A-site forces an equivalent occupation of the B-site by Mn^{3+} and Mn^{4+} ions, producing, at <175 K, a charge (and orbital) ordering scheme that is described by the *I*2/*m* monoclinic symmetry.[10] A distorted coordination, resulting from an unusual occupation of $d_{x^2-y^2}$ orbitals is detected for Mn^{3+}, while, as expected, the Jahn−Teller inactive Mn^{4+} ion does not show any distortion. The delocalization of the Mn^{3+} e_g electrons on the B-site, taking place above 175 K, yields the melting of charge and orbital orderings and increases the symmetry to cubic (space group *Im*3); all the undistorted Mn B ions become symmetry equivalent, pointing out the fundamental role of the ordering phenomena in defining the crystal structure. A bivalent ion on the A-site induces a 3:1 Mn^{3+}:Mn^{4+} ratio over the B-site, forcing the symmetry to become rhombohedral ($R\bar{3}$) in the charge-ordered phase, as in the case of $CaMn_7O_{12}$ the undistorted Mn^{4+} site lays on the

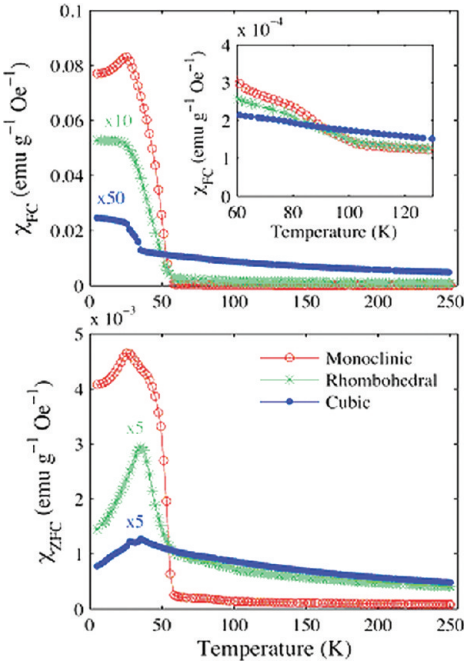

Figure 7. $\chi(T)$ ZFC-FC measurements in 10 Oe for the monoclinic (red), rhombohedral (green), and cubic (blue) polymorphs. (The lower panel shows ZFC data, while the upper panel shows FC data.) The inset shows the detail of the FC $\chi(T)$ plot in the region affected by $BiMnO_3$ impurities.

rhombohedral 3-fold axis, while the Mn^{3+} ions, characterized by the occupation of the $d_{z^2-r^2}$ orbitals, lay around it.[15] The presence of a trivalent ion on the A-site involves the sole presence of Mn^{3+} ions within the structure. Despite this, the structure of $LaMn_7O_{12}$ is once again monoclinic; in this case, the $I2/m$ symmetry is related to the description of the particular $d_{x^2-y^2}$ orbital ordering scheme.[16] In $LaMn_7O_{12}$, the monoclinic symmetry is retained up to 653 K, where the cubic $Im\bar{3}$ symmetry sets in, as the charge localization and orbital ordering are lost.[17] The praseodymium(III)-substituted member of the series follows this rule of thumb and presents a monoclinic structure; however, this compound also crystallizes in a rhombohedral polymorph, in which the presence of low-spin Mn^{3+} ions was claimed to explain the detection of undistorted octahedra sitting on the $\bar{3}$ symmetry site.[18] As for the lanthanum compound, the structure of $BiMn_7O_{12}$ is monoclinic and the orbital ordering scheme of the B-sites that can be derived from the Mn−O bond distances is the same as that observed in $LaMn_7O_{12}$, despite the acentric character of the structure. However, the introduction of a few percent of Mn^{4+} in the structure is able to progressively increase the symmetry to rhombohedral and then to cubic. Evidently, the Mn^{4+} doping perturbs the orbital ordering of the B sites. As discussed previously, the rhombohedral symmetry agrees with the localization of Mn^{4+} on a specific B-site (the one on the 3-fold axis), whereas a further increase of its content induces a complete delocalization, resulting in a cubic symmetry. In light of the present results, a partial oxidation of manganese on the B-site should be taken into account to explain the symmetry change observed in $PrMn_7O_{12}$ and the partial oxidation of the corresponding La-phase should be attempted to verify the general nature or the specific nature of the phenomenon.

3.3. Magnetic Characterization. Figure 7 shows $\chi(T)$ ZFC−FC curves, in an applied field of 10 Oe, for the monoclinic, rhombohedral, and cubic polymorphs. Considering the monoclinic phase, the sample clearly displays two different transition temperatures ($T_{A'}$ = 22 K and T_B = 55 K), with the development of a small net magnetic moment at low temperature, because of Dzyaloshinskii−Moriya (DM) interaction. The nature of the two transitions is antiferromagnetic (AFM), as confirmed by the negative paramagnetic Curie temperature (θ_p = −143 K). Effective magnetic moment value for Mn(III) in the structure has also been extrapolated and turns out to be 5.3 μ_B. The critical temperatures $T_{A'}$ and T_B can be related to the ordering of Mn ions in square planar and octahedral sublattices respectively. This is supported not only by the analogy with $LaMn_7O_{12}$ (ref 16) but also by structural symmetry reasons. DM interaction, in fact, is an antisymmetric exchange interaction of the form $D\cdot(\mathbf{S_i} \times \mathbf{S_j})$ between two spins $\mathbf{S_i}$ and $\mathbf{S_j}$, giving rise to a nonzero net result only when the midpoint between $\mathbf{S_i}$ and $\mathbf{S_j}$ is not a center of inversion; this is the case of the tilted octahedra in $BiMn_7O_{12}$. For the rhombohedral phase, a single transition temperature is obtained from ZFC−FC curves at T_B = 35 K that can be attributed to the ordering of octahedral B-sites in analogy with the considerations presented for the monoclinic phase. Curie−Weiss fitting was performed also for this polymorph giving a θ_p value of −103.9 K and an effective magnetic moment for Mn(III) of 5.13 μ_B. The negative Curie paramagnetic temperature suggests that the transition at T_B is antiferromagnetic, with the development of a net magnetic moment due to DM interaction one order of magnitude lower, with respect to the monoclinic phase. Considering now ZFC−FC curves for the cubic polymorph, they display a clear AFM transition temperature, T_B = 33 K, characterized by a negative θ_p value, and a hardly distinguishable transition at a lower temperature (24 K). Also in this case, at T_B, a net magnetic moment, 2 orders of magnitude smaller compared to the monoclinic phase, arises, likely because of the ordering of the tilted octahedral sites. Curie−Weiss fitting leads, in this case, to an effective magnetic moment for Mn(III) of 5.33 μ_B. Comparing the three values obtained for the three polymorphs, no evident modifications of the Mn(III) effective magnetic moment can be correlated to the different bismuth deficiency. Looking at the magnified view of $\chi(T)$ curves, shown in the inset of Figure 7, the presence of two anomalies, at 80 and 100 K, can be seen in all three polymorphs, which can be ascribed to the presence of $BiMnO_3$ impurities, that undergo a ferromagnetic transition at these temperatures.[19,20] Before performing $M(H)$ measurements at T = 5 K, which is below the AFM ordering temperatures of the three considered polymorphs, magnetic hysteresis loops were measured with ΔH = ±50 kOe at an intermediate temperature of 65 K in order to exclude any contribution of the detected impurities of $BiMnO_3$, as confirmed by the observed simple paramagnetic behavior (see Figure S2 in the Supporting Information). Figures 8a and 8b show $M(H)$ measurements at 5 K with ΔH = ±50 kOe, in the magnetic ordered state, for the monoclinic and rhombohedral phase. In the case of the monoclinic polymorph, a large major loop appears with a coercive field of H_c = 14.1 kOe and with a remnant magnetization value of 1.624 emu/g. This quantity is defined here as the applied magnetic field value at which the first derivative of the hysteresis loop branch displays its maximum. This irreversible contribution turns out to be superimposed to a dominant reversible one attributed to the main antiferromagnetic nature of the system, as confirmed by the susceptibility high field measurements reported in Figure S3 in the Supporting Information. For this reason, care must be taken in considering M_s values for

the three polymorphs, which are affected by this signal. Also, in the case of the rhombohedral sample, a loop opens, showing a larger paramagnetic contribution, with H_c = 12.8 kOe and with a remnant magnetization value of 1.263 emu/g slightly smaller than that measured for the monoclinic phase. The detected values are quite unusual for DM weak ferromagnets, which usually exhibit coercive fields orders of magnitude lower, as in the case of $LaMn_7O_{12}$.[16] The possible extrinsic character of the phenomenon was ruled out by the measurement of $M(H)$ curves on randomly oriented single-crystal samples, not showing relevant changes with respect to the polycrystalline ones. As a consequence, interactions of different nature, such as homogeneous and inhomogeneous magneto-electric effect, must be taken into account to explain the anomalously large coercive field values that are detected.[21] In fact, in the case of different antiferromagnetic ferroelectrics, such as $BiFeO_3$, the pinning of AFM domain walls to ferroelectric (FEL) ones has been observed,[22,23] as well as the presence of an irreversible magnetization process due to magneto-electric coupling. This is suggested also taking into account the $M(H)$ measurement performed in the magnetic ordered state for the cubic polymorph (which is not macroscopically ferroelectric) shown in Figure 8c, exhibiting an almost vanishing hysteresis with H_c = 1.2 kOe and an M_r value much smaller than those previously discussed for the monoclinic and rhombohedral samples (0.408 emu/g). The most relevant results of the magnetic characterizations performed on the three polymorphs are reported in Table 2. The relationship between magnetic coercivity and electric domains is made clearer by considering TEM and HREM measurements also, suggesting the presence of FEL stripe domains more evident in the monoclinic phase than in the rhombohedral one exhibiting a lower coercive field value. In contrast, the cubic polymorph, with a vanishing hysteresis, presents no clear sign of domains related to electric dipoles. Unfortunately, the direct measurement of $P(E)$ hysteresis loops, which would represent the evidence of the FEL behavior of the monoclinic and rhombohedral polymorphs, is made quite difficult, as for many multiferroics, by their semiconducting behavior, which prevents reliable dielectric measurements at RT. The intergranular semiconductivity effects, just evidenced for $LaMn_7O_{12}$, lead to a RT resistivity of ~40 Ω cm,[16] which is a condition that leads to loss currents far greater than those arising from polarization processes. Reducing the temperature by ~100 K allows one to gain a high resistivity of the sample, on the order of 10^{11} Ω cm. However, at this temperature, the really poor dielectric strength of helium gas that limits the applied voltage to 150 V not sufficient to get well-saturated data useful to distinguish irreversible contributions from spurious ones, as reported in ref 24. However, we performed pyroelectric current measurements, which reveal a polarization inversion under the inversion of the poling field.

Moreover, dielectric constant measurements, reported as Figure S4 in the Supporting Information show clear anomalies at the magnetic ordering temperatures in the monoclinic polymorph, confirming the possible existence in these compounds of magneto-electric coupling.

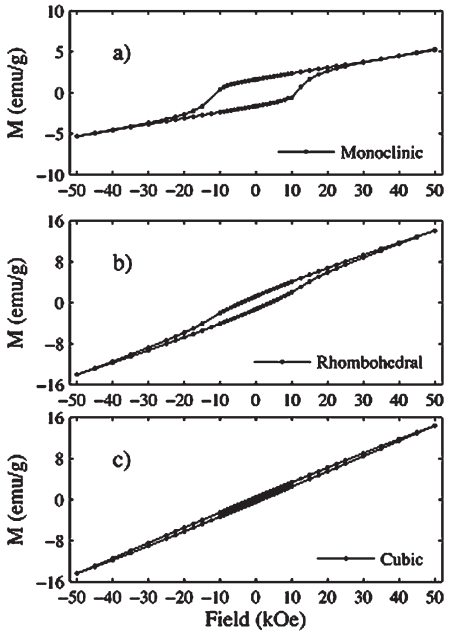

Figure 8. $M(H)$ measurements in $\Delta H = \pm 50$ kOe for the (a) monoclinic, (b) rhombohedral, and (c) cubic polymorphs.

4. CONCLUSIONS

Relevant structural changes producing large variations of the physical properties are induced by subtle changes of the global stoichiometry (related to the partial oxidation of manganese) on the quadruple perovskite $Bi_{1-x/3}(Mn^{III}{}_3)(Mn^{III}{}_{4-x}Mn^{IV}{}_x)O_{12}$. For x values ranging from 0 to 0.1, the monoclinic phase, which already is known for the stoichiometric composition and determined by the orbital ordering of the B-sites, is formed. No relevant modification of the physical properties, with respect to the stoichiometric phase is observed, so that weak ferromagnetism induced by DM interaction coexists with polar properties related to the loss of inversion symmetry. When samples are prepared with composition in the range $0.10 < x < 0.27$, the structural symmetry changes from monoclinic to rhombohedral, as a consequence of the partial loss of orbital ordering involving localization of Mn^{4+} on the B-site lying on the 3-fold axis. Single-crystal XRD studies and TEM measurements suggest also this structure to be ferroelectric, with the Bi atoms shifted off the inversion center along the [111]-direction of the rhombohedral crystallographic cell. Finally, for x values of >0.27, the delocalization of Mn^{4+} produces the complete melting of the Mn^{3+} orbital ordering, resulting in a cubic phase. Although its average structure could be described in the centrosymmetric $Im3$ space group, the Bi atoms are statistically shifted out of the inversion center, suggesting local polar properties. Even if the Mn^{4+} content can vary within a single polymorph, the variation is so limited that the magnetic behavior depends critically only on the

Table 2. Summary of Magnetic Properties for the Three Considered Polymorphs

sample	$T_{A'}$(K)	T_B(K)	θ_P (K)	p_{eff} (μ_B)	χ_{5K} (emu g^{-1} Oe^{-1})	H_c (kOe)	M_r (emu g^{-1})	M_s (emu g^{-1})
monoclinic	22 ± 0.5	50 ± 0.5	−143.3 ± 0.6	5.3 ± 0.1	(7.7 ± 0.4) × 10^{-2}	14.1 ± 0.1	1.624 ± 0.004	5.22 ± 0.04
rhombohedral		35 ± 0.5	−103.9 ± 0.4	5.13 ± 0.06	(5.3 ± 0.3) × 10^{-3}	12.8 ± 0.1	1.263 ± 0.002	14.44 ± 0.01
cubic	24 ± 0.5	33 ± 0.5	−90.4 ± 0.5	5.33 ± 0.05	(5 ± 0.3) × 10^{-4}	1.2 ± 0.1	0.408 ± 0.002	14.03 ± 0.01

dx.doi.org/10.1021/cm200879p |Chem. Mater. 2011, 23, 3628–3635

crystal symmetry. Consequently, the magnetic behavior can be considered as the characteristic signature of the polymorphs. This applies in particular to the $M(H)$ measurements, giving rise to hysteresis loops having structure-dependent shape and characteristics. The hysteresis loops reflect, in all cases, the complex nature of the magnetic response: on one side, the ferromagnetic (FM) nature of the Dzyaloshinskii−Moriya (DM) interaction is responsible of the observed hysteresis; on the other hand, the antiferromagnetic (AFM) nature of the magnetic ordering prevents saturation. The loop is very narrow for the cubic phase, and it becomes wider and wider, passing to rhombohedral and monoclinic, at the same time increasing the tendency to saturate. Really surprising are the huge values of the coercive field of the rhombohedral and monoclinic phases, exceeding 10 kOe. Similar values are characteristic of hard magnetic materials, characterized by a large magnetic anisotropy and appear absolutely unrealistic for a weak DM ferromagnet. The unique way to explain the phenomenon is to assume a very efficient pinning process that opposes to the reversal of the magnetic polarization. By taking into account that, at least for the monoclinic phase, anomalies in the dielectric characterization have been observed at the magnetic ordering temperatures $T_{A'}$ and T_B,[7] the suggested existence of magnetoelectric coupling could be considered the origin of the measured coercive field. In this case, the magnetic domains would be pinned to the electric ones, so that the latter oppose to the inversion of the magnetic polarization. This hypothesis finds further support in the behavior of the cubic phase, where, despite the local polar character, ferroelectric properties are prevented by its centrosymmetric structural character.

■ ASSOCIATED CONTENT

Supporting Information. Description of the material included. Comparison of the PXRD patterns of the three $BiMn_7O_{12}$ phases is shown (Figure S1). Crystal CIF data, refinement parameters refined atomic parameters, relevant bond distances for both the rhombohedral and cubic polymorphs are reported (Tables S1−S6). $M(H)$ measurements performed above the $BiMn_7O_{12}$ magnetic ordering transitions are reported (Figure S2), and high field susceptibility for the monoclinic polymorph is reported (Figure S3). Dielectric permittivity as a function of temperature is reported for the monoclinic and rhombohedral phases (Figure S4). This material is available free of charge via the Internet at http://pubs.acs.org.

■ AUTHOR INFORMATION

Corresponding Author
*E-mail: francesco.mezzadri@unipr.it.

■ REFERENCES

(1) Schmid, H. *Ferroelectrics* **1994**, *162*, 317.
(2) Kimura, T.; Goto, T.; Shintani, H.; Ishizaka, K.; Arima, T.; Tokura, Y. *Nature* **2003**, *426*, 55.
(3) Hur, N.; Park, S.; Sharma, P. A.; Ahn, J. S.; Guha, S.; Cheong, S.-W. *Nature* **2004**, *429*, 392.
(4) Blake, G. R.; Chapon, L. C.; Radaelli, P. G.; Park, S.; Hur, N.; Cheong, S.-W.; Rodrìguez-Carvajal, J. *Phys. Rev. B* **2005**, *71*, 214402.
(5) Moreira dos Santos, A. F.; Cheetham, A. K.; Atou, T.; Syono, Y.; Yamaguchi, Y.; Ohoyama, K.; Chiba, H.; Rao, C. N. R. *Phys. Rev. B* **2002**, *66*, 064425.
(6) Van Aken, B. B.; Palstra, T. T. M.; Filippetti, A.; Spaldin, N. A. *Nat. Mater.* **2004**, *3*, 164.
(7) Imamura, N.; Karppinen, M.; Yamauchi, H. *Chem. Mater.* **2009**, *21*, 2179.
(8) Mezzadri, F.; Calestani, G.; Calicchio, M.; Gilioli, E.; Bolzoni, F.; Cabassi, R.; Marezio, M.; Migliori, A. *Phys. Rev. B* **2009**, *79*, 100106.
(9) Marezio, M.; Dernier, P. D.; Chenavas, J.; Joubert, J. C. *J. Solid State Chem.* **1973**, *6*, 16.
(10) Prodi, A.; Gilioli, E.; Gauzzi, A.; Licci, F.; Marezio, M.; Bolzoni, F.; Huang, Q.; Santoro, A.; Lynn, J. W. *Nat. Mater.* **2004**, *3*, 48.
(11) Imamura, N.; Karppinen, M.; Motohashi, T.; Fu, D.; Itoh, M.; Yamauchi, H. *J. Am. Chem. Soc.* **2008**, *130*, 14948.
(12) Burla, M. C.; Caliandro, R.; Camalli, M.; Carrozzini, B.; Cascarano, G. L.; De Caro, L.; Giacovazzo, C.; Polidori, G.; Spagna, R. *J. Appl. Crystallogr.* **2005**, *38*, 381.
(13) Sheldrick, G. M. *Acta Crystallogr., Sect. A: Found Crystallogr.* **2008**, *64*, 112.
(14) Subramanian, M. A.; Sleight, A. W. *Solid State Sci.* **2002**, *4*, 347.
(15) Bochu, B.; Chenavas, J.; Joubert, C.; Marezio, M. *J. Solid State Chem.* **1974**, *11*, 88.
(16) Prodi, A.; Gilioli, E.; Cabassi, R.; Bolzoni, F.; Licci, F.; Huang, Q.; Lynn, J.-W.; Affronte, M.; Gauzzi, A.; Marezio, M. *Phys. Rev. B* **2009**, *79*, 085105.
(17) Okamoto, H.; Karppinen, M.; Yamauchi, H.; Fjellvåg, H. *Solid State Sci.* **2009**, *11*, 1211.
(18) Mezzadri, F.; Calicchio, M.; Gilioli, E.; Cabassi, R.; Bolzoni, F.; Calestani, G.; Bissoli, F. *Phys. Rev. B* **2009**, *79*, 014420.
(19) Montanari, E.; Righi, L.; Calestani, G.; Migliori, A.; Gilioli, E.; Bolzoni, F. *Chem. Mater.* **2005**, *17*, 1765.
(20) Belik, A. A.; Kodama, K.; Igawa, N.; Shamoto, S.; Kosuda, K.; Takayama-Muromachi, E. *J. Am. Chem. Soc.* **2010**, *132*, 8137.
(21) Gaareva, Z. V.; Zvezdin, A. K. *Europhys. Lett.* **2010**, *91*, 47006.
(22) Meier, D.; Maringer, M.; Lottermoser, Th.; Becker, P.; Bohaty, L.; Fiebig, M. *Phys. Rev. Lett.* **2009**, *102*, 107202.
(23) Fiebig, M.; Lottermoser, Th.; Fröhlich, D.; Goltsev, A. V.; Pisarev, R. V. *Nature* **2002**, *419*, 818.
(24) Scott, J. F. *J. Phys.: Condens. Matter* **2008**, *20*, 021001.